AIAA JOURNAL
Vol. 40, No. 3, March 2002

Parametric Study of Heat Release Preceding a Blunt Body in Hypersonic Flow

Ryoji Takaki* and Meng-Sing Liou†
NASA John H. Glenn Research Center at Lewis Field, Cleveland, Ohio 44135

A computational parametric study is presented illustrating the effects of upstream heat release on drag and heating rate in hypersonic flow over an axisymmetric blunt body. A chemical nonequilibrium viscous flow is considered with seven species; Park's two-temperature model is also used to take account of thermally nonequilibrium phenomena. Three parameters that control the heat release are introduced, and their effects on the flow structure, specifically with respect to drag and heating rate, are quantified. Results show that heat release upstream of the body can reduce not only the aerodynamic drag but also the aerodynamic heating rate at the body surface. Computed results achieved a reduction of 23% in drag and 74% in heating rate, relative to baseline values in the absence of heat release. The reduction mechanism is discussed, and dynamic pressure is shown to play an important role in the drag reduction mechanism.

Nomenclature

C_D	=	drag coefficient of the hemisphere [see Eq. (3)]
C_{D0}	=	C_D without heat release
E	=	energy, J/m^3
E_c	=	coefficient to the amount of the heat source [see Eq. (2)]
F_x	=	drag component of pressure and skin friction [see Eq. (3)]
$G(x, r)$	=	Gaussian function [see Eq. (1)]
L	=	characteristic length of the heat source, m [see Eq. (1)]
M_∞	=	freestream Mach number
p	=	pressure, Pa
p_t	=	total pressure behind a normal shock, Pa [see Eq. (9)]
p_θ	=	pressure at the surface, indicated by θ, Pa [see Eq. (9)]
$\dot{Q}$	=	amount of the heating rate of the hemisphere, MW [see Eq. (3)]
$\dot{Q}_{\text{in}}$	=	energy supplied per unit volume per unit time, J/m^3/s [see Eq. (2)]
$\dot{Q}_0$	=	$\dot{Q}$ without heat release
$\dot{q}$	=	heat flux, MW/m^2 [see Eq. (4)]
q_∞	=	freestream dynamic pressure, Pa
R	=	radius of the hemisphere ($R = 1.0$), m [see Eq. (2)]
R_e	=	Reynolds number
S	=	surface of the hemisphere [see Eq. (3)]
S_0	=	cross-section area of the hemisphere, m^2 [see Eq. (3)]
T	=	temperature (translational and rotational), K
T_V	=	vibrational temperature (vibrational and electron excitational), K
T_{wall}	=	wall temperature ($T_{\text{wall}} = 1200$), K
V_∞	=	freestream velocity, m/s
x, r	=	cylindrical coordinates, m
x_c, r_c	=	position of the heat source, m [see Eq. (2)]
γ	=	ratio of specific heats
Δ	=	difference between the value and the value without heat release [see Eq. (6)]
θ	=	incidental angle between the freestream velocity and the normal vector of the surface [see Eq. (9)]
π	=	circular constant
ρ	=	density

Subscript

∞	=	freestream value

Received 25 July 2000; revision received 29 May 2001; accepted for publication 7 September 2001.

*Research Associate, Institute for Computational Mechanics in Propulsion; currently Senior Researcher, CFD Technology Center, National Aerospace Laboratory, Tokyo 182-8522, Japan. Member AIAA.

†Senior Scientist, Turbomachinery and Propulsion Systems Division. Associate Fellow AIAA.

Introduction

ONE of the most important aspects of designing a hypersonic flight vehicle like a reentry vehicle is how to manage the extremely severe thermal environment. To protect vehicles from the severe thermal environment, designers use various thermal protection systems, such as cooling systems or nose shapes, to reduce the aerodynamic heating rate. Carbon fibers or ceramic tiles have been used as a thermal protection system, but the surface temperature due to the aerodynamic heating might easily exceed the temperature that these materials can withstand. On the other hand, although the cooling system can decrease the surface temperature easily, it requires the release or emission of additional cold fluid, thereby increasing the weight of the vehicles and consequently decreasing the amount of payload. The adaptation of the blunt nose shape is the simplest and the most effective method and has been widely used in designing hypersonic flight vehicles. Although a large-radius nose can reduce the aerodynamic heating, it also increases the aerodynamic drag. As a result, greater thrust power and more fuel are necessary, leading to reduced payloads. Therefore, a great deal of research has focused on how to reduce the aerodynamic drag for the blunt-body configuration. One innovative approach is to put a physical spike on the nose, as conducted by several researchers.[1–4] Although the physical spike can reduce the aerodynamic drag significantly, it generates severe thermal stress and requires cooling, thereby compromising the advantages. Historically, engineering tradeoff has been practiced between reducing the aerodynamic heating and reducing the aerodynamic drag.

Recently, a new concept, as depicted in Fig. 1, has been proposed to reduce the aerodynamic drag of a blunt body in high-speed flight (not only hypersonic flight but also supersonic flight). A heat source placed in front of the blunt body acts in the same way as a physical spike nose. The heat release might be supplied by electromagnetic or other means (lasers, microwaves, combustion, etc.). It can change the shock shape or generate another shock in front of the body, depending on where and how the energy input is distributed. This nonstructural energy spike (energy release in front of the body) can generate similar or greater drag reduction than that obtained by a structural spike.

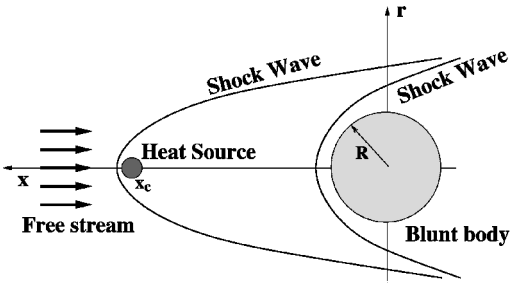

Fig. 1 Flow with a heat release in front of the body.

The possibility of achieving drag reduction with a heat source in front of a blunt body has been pioneered by Myrabo and Raizer[5]: this particular experimental study used a protruding physical spike with a plasma torch. They reported the effect of the heat source by comparing the flow with the spike and the flow with the heated spike. They named this concept "laser-induced air spike" or "directed-energy air spike." They also proposed an advanced transatmospheric vehicle, and they have demonstrated light-craft flight experiments by utilizing an innovative propulsion system.

Computational studies for this concept have been performed by a number of researchers by solving the Euler[6,7] and Navier–Stokes equations with a perfect gas model.[8,9] However, two important issues have not been addressed in these studies: 1) nonequilibrium (thermal or chemical) effects in the high-temperature regime (high-temperature effects) and 2) the aerodynamic heating rate. Therefore, in this study we shall numerically investigate the hypersonic flow around a hemisphere with upstream heat release including high-temperature effects, focusing on the flow structure (especially the shock configuration) and understanding of these physical phenomena. Moreover, we shall attempt to find optimum conditions to reduce aerodynamic drag as well as heating rate.

Numerical Methods

We give a brief summary of the numerical method used for the present study; details can be found in Refs. 10 and 11. Prior to a systematic parametric study, validation and verification of the computational fluid dynamics (CFD) code has been conducted to determine appropriate grid spacings required for an accurate prediction of heat transfer.

Physical Models

We will consider axisymmetric, steady, and laminar flows throughout this study. As a chemical reaction model, we consider seven chemical species—O_2, N_2, N, O, NO, NO^+, and e^-—and 18 finite-rate chemical reactions. Park's model is used to calculate forward and backward reaction-rate constants. As a thermal mode, we consider Park's two-temperature model.[12,13] This model uses two kinds of temperature, in other words, assuming two kinds of internal energy mode. The translational and rotational energy modes are considered to be in an equilibrium state, and they are represented by translational temperature T or temperature in short. The vibrational and electron excitational energy modes are considered to be in another equilibrium state, and they are represented by vibrational temperature T_V. As a relaxation model between the vibrational and translational mode, we use Millikan and White's semi-empirical model,[14] which is based on the Landau–Teller theory. However, this model is known to underestimate the vibrational relaxation time when the translational temperature is more than about 8000 K. Therefore Park's modified model,[15] which limits particle collisions at high temperatures, is also used.

Numerical Schemes

A finite volume formulation is used to approximate the Navier–Stokes equation with the preceding physical and chemical models. The AUSMDV[16,17] scheme, which is one of the AUSM family schemes, is used to construct numerical flux for inviscid terms at cell faces. The MUSCL approach is used to achieve higher-order evaluation of the numerical flux, and the minmod limiter used to avoid numerical oscillations around discontinuities. The second-order central-differencing scheme is used for viscous terms. The lower–upper alternative direction implicit (LU-ADI) method with the local time-stepping method is used for time integration. Finally, we use the point-implicit method to approximate the source terms representing nonequilibrium effects.

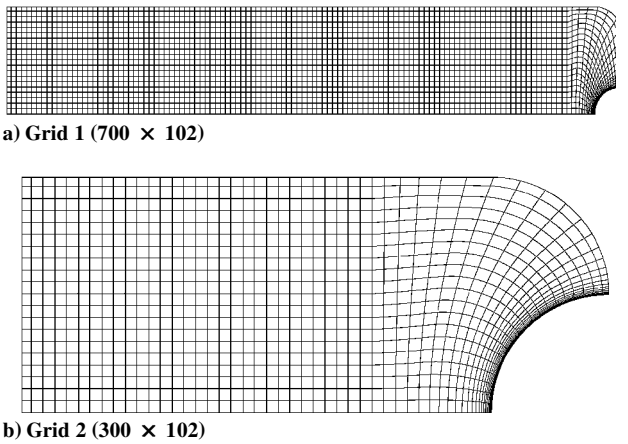

a) Grid 1 (700 × 102)

b) Grid 2 (300 × 102)

Fig. 2 Computational grid.

Heat Source

A Gaussian distribution

$$G(x, r) = \left(1 \Big/ 2\pi\sqrt{2\pi}L^3\right) \exp[-(x^2 + r^2)/2L^2] \qquad (1)$$

is used to give a mathematical representation of the heat source

$$\dot{Q}_{\text{in}} = \pi R^2 E_\infty V_\infty E_c \times G(x - x_c, r - r_c) \qquad (2)$$

Three parameters are used to control heat release. The first is the position of the heat source, described by (x_c, r_c). Because symmetric flow is considered in this investigation, the heat source is required to be located on the symmetric axis. This leads to setting $r_c = 0$. The second is the effective length of the heat source, denoted by L, which controls the size of the heat source. The last, denoted by E_c, is the coefficient to control the intensity of heat supplied. As a reference to determine the amount of heat supplied, we shall use the amount of freestream energy that passes through the hemisphere per unit time $(\pi R^2 E_\infty V_\infty)$. Therefore, the parameter E_c is the coefficient to this reference energy.

Computational Grid

Figure 2 shows the computational grids for a symmetric flow around a hemisphere whose radius R is 1.0 m. Figure 2a shows the grid for large values of the parameter x_c, and Fig. 2b is the grid for a moderate value of $x_c = 4.0$. Both grids are denoted respectively as grids 1 and 2. The number of grid points in the flow direction (x direction) is 700 for grid 1 and 300 for grid 2. The number of grid points transverse to the flow direction (r direction) of both grids is 102. The computational grid in the upstream region ($x < 2.0$) becomes a Cartesian grid in order to avoid grid distortion. As the heat-flux prediction is extremely sensitive to the grid resolution, a grid convergency check should be carried out. For this purpose the grid, with cell Reynolds number equal to about 21.0, is judged to be adequate for our calculations.

Calculation Conditions

As a calculation condition, we select one point from a typical trajectory of reentry vehicles.[5] The altitude is 48 km, and Mach number is about 14, which yields Reynolds number about 0.3×10^6. Details are listed in Table 1. The wall temperature T_{wall} is fixed at 1200 K, and a noncatalytic wall is assumed. As described before, we consider three parameters to characterize the energy release, and each value is listed in Table 2. Because the three parameter x_c, L, and E_c are independent, the parameter x_c is examined separately in this work. When we change the parameter x_c, which is described in group 1 of Table 2, the parameter E_c is fixed, but the parameter L

varies, taking values of 0.1, 0.2, and 0.4. Grid 1 is used for this case. When changing the parameters L and E_c, described in group 2 of Table 2, the parameter x_c is fixed to 4.0. Grid 2 is used for this case. Table 3 shows the matrix of calculated cases for group 2, where the parameter x_c is fixed to 4.0. The symbol ◯ shows calculated cases, and the symbol × shows a condition, which was calculated but experienced problems that will be described later.

Results

In this section computed results are shown. First, the structure of the flow with heat release is presented. Then, aerodynamic characteristics, specifically aerodynamic drag and aerodynamic heating, will be presented, together with discussion on the effects on both characteristics by the parameters associated with the input heat source. Finally, the effects of high temperature relative to the perfect gas assumption are studied.

Flow Structure

First, we show the general structures of the flow with heat release, whose parameters are $x_c = 4.0$, $L = 0.2$, and $E_c = 0.05$. Of course, the flow structure will be different with different values of each parameter. We shall see contours of flow variables, followed by the distributions along the symmetric axis and along the surface.

Figure 3 gives the contours of both temperatures (T and T_V), pressure, and Mach number for the flow with heat release. Figure 4 also shows the stream lines at the bow shock layer. Because of the heat release and the associated change of gas states in the region, an apparent body is seen by the incoming flow, resulting in compression waves around the heat release region. These compression waves converge to a strong shock wave behind the heat source, and it subsequently propagates downstream (Fig. 3c). We call this shock *primary shock*. This primary shock wave causes a shock-shock interaction with the original bow shock, which exists in front of the hemisphere, and we call it *secondary shock* or *bow shock*. As a result of the shock-shock interaction, the shape of the bow shock and the structure of the flow in the bow shock layer are altered. A contact surface can be seen between the bow shock and the body surface (Fig. 3a). This contact surface is a boundary of recirculation regions shown in Fig. 4 (two recirculation regions can be seen in the bow shock layer). Temperature layers, caused by the heat release (mainly coming from the Gaussian distribution of the input energy), can also be seen in the temperature contours (Figs. 3a and 3b). This

Table 1 Freestream conditions

Parameter	Value
Temperature T_∞	264.078 K
Pressure p_∞	68.47 Pa
Velocity V_∞	4550 m/s
Mach number M_∞	13.92
Reynolds number R_e	2.65×10^5
Wall temperature T_{wall}	1200 K
Wall catalyticy	Noncatalytic wall

Table 2 Parameters

Parameter	Group 1 (x_c)	Group 2 (L and E_c)
x_c	2, 4, 6, 8, 10 12, 14, 16 18, 20, 22	4
L	0.1, 0.2, 0.4	0.03, 0.05, 0.07, 0.08 0.1, 0.12, 0.13, 0.15 0.2, 0.25, 0.3, 0.4
E_c	0.01	0.00001, 0.0001, 0.001 0.005, 0.01, 0.05 0.1, 0.2, 0.5, 1.0, 10

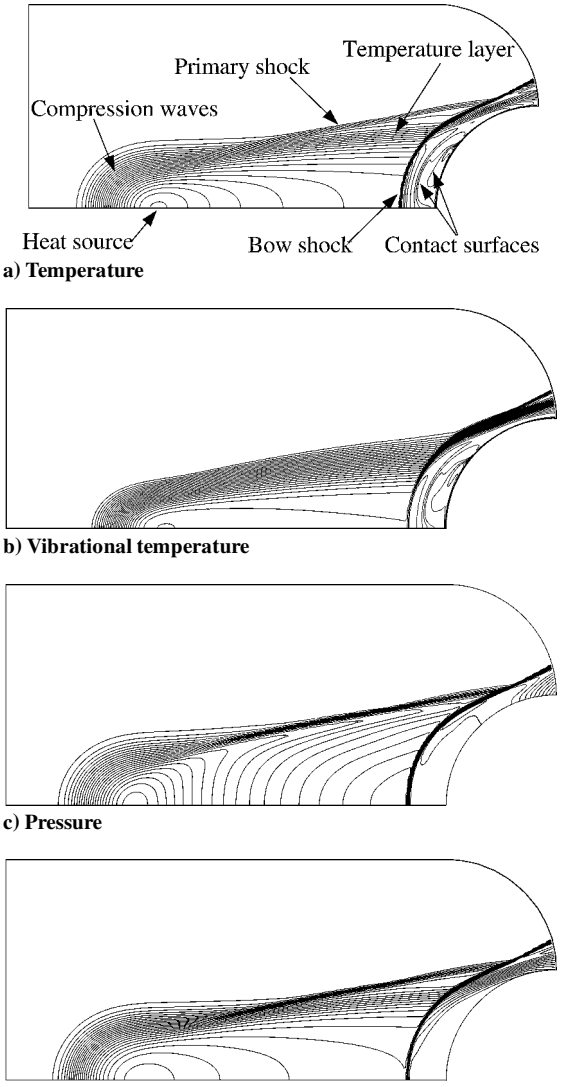

a) Temperature

b) Vibrational temperature

c) Pressure

d) Mach number

Fig. 3 Contours of a flow with a heat release.

Table 3 Calculated conditions (group 2, $x_c = 4.0$)

	E_c										
L	0.00001	0.0001	0.001	0.005	0.01	0.05	0.1	0.2	0.5	1.0	10.0
0.4			◯		◯	◯	◯	◯	◯	◯	×
0.3			◯		◯						
0.25			◯		◯	◯					
0.2		◯	◯	◯	◯	◯	×		×	×	×
0.15			◯		◯	◯					
0.13					◯						
0.12					◯						
0.1		◯	◯		◯		×		×	×	
0.08			◯								
0.07			◯								
0.05		◯	◯		◯		×				
0.03	◯	◯	◯		×						

temperature layer impinges on the bow shock and changes its shape. As the flow goes through these two shocks, a peak value in surface pressure might appear, as seen in the results.

Figure 5 compares the effects of a heat release on the distributions of several variables along the symmetric axis. In these figures the horizontal scales are different. Regarding the flow with the heat release, both temperatures and pressure increase while Mach number decreases rapidly in the heat release region. Behind the heat source both temperatures and pressure decrease, and Mach number increases gradually until reaching the bow shock. The relaxation process between the vibrational mode and the translational mode can be seen in the heat release region in Fig. 5b. However, behind the heat release region the relaxation process seems to terminate because the distribution of vibrational temperature does not follow that of the temperature. Moreover, the vibrational temperature becomes higher than the translational temperature in front of the bow shock. Therefore, the flow behind the heat release region becomes a frozen flow, similar to a strongly expanding flow. This fact (the flow becomes frozen behind the heat release region) will be further mentioned in the following discussion about chemical reactions. The values of all variables in front of the bow shock are different from those without heat release. Therefore, the values behind the bow shock are also different from those of the flow without the heat release. Also, the bow shock layer of the flow without heat release is thinner than that of the flow with heat release, roughly 0.09 vs 0.4.

Figure 6 shows mole fraction distributions for the chemical species along the symmetric axis (again, the horizontal scales are different). Regarding the flow with heat release, strong chemical reactions are seen, in Fig. 6b, to occur in the heat release region and just behind the bow shock. Species O_2 and N_2 are partially dissociated, producing O and NO. The flow behind the heat source becomes a frozen flow (the mole fractions of each species remain constant). This fact also can be seen in Fig. 5b, as mentioned before.

Figure 7 shows the pressure and heat-flux distributions along the hemisphere surface. The horizontal axis represents the angle measured from the stagnation point. In the case of the flow without heat release, both pressure and heat flux show the similar behavior, having the maximum values at the stagnation point and decreasing monotonically away from it. However, in the case of flow with heat release (Fig. 7) the peak in both variables shifts to the outer region, and their values become smaller than that in the flow without heat release. Also both values have almost a flat distribution around the stagnation region. From these facts a reduction in pressure drag and surface heating rate can be expected. In particular, the pressure drag will decrease dramatically as a result of a combination of the following two factors: 1) significant decrease in pressure on most of the surface and 2) shift of the peak position to the outer region. The second factor means that the pressure component in the flow direction, which works as the drag, decreases because the angle between the normal direction of the surface and the direction of the

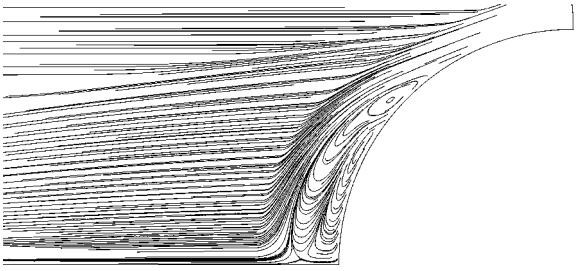

Fig. 4 Streamlines of a flow with a heat release.

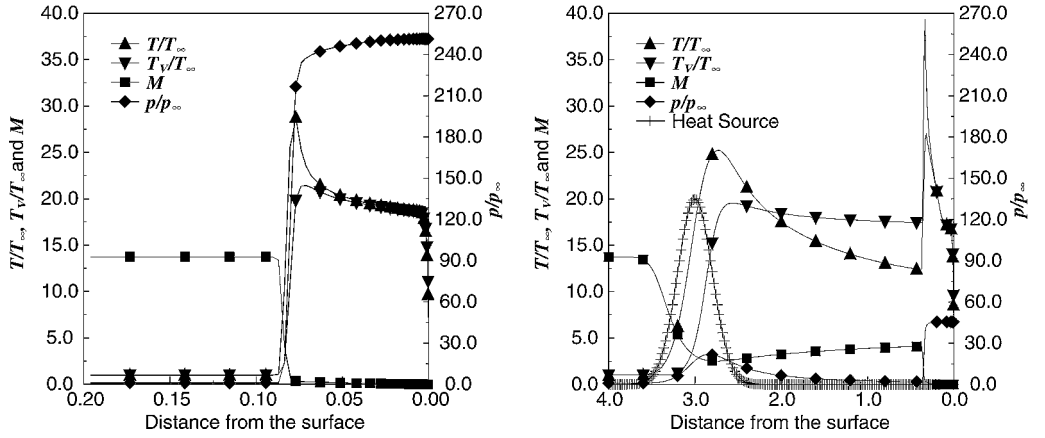

a) Without Q_{in} **b) With Q_{in}**

Fig. 5 Distributions of several values along the symmetric line.

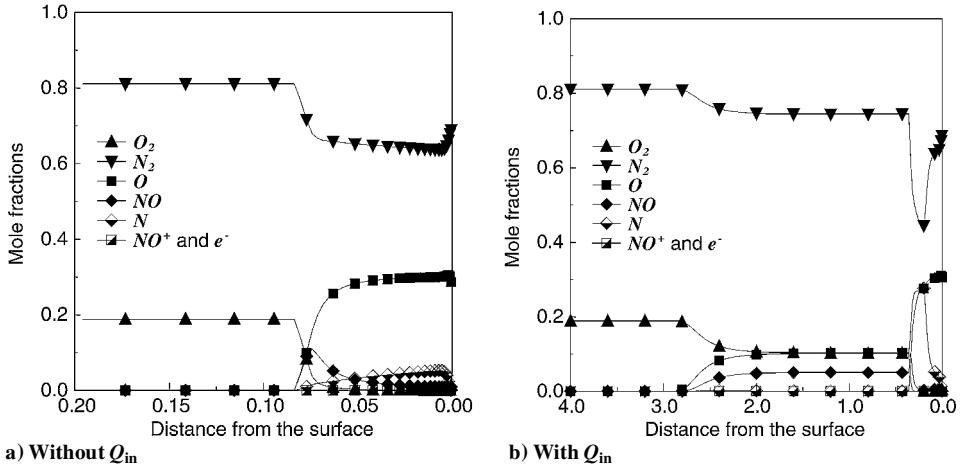

a) Without Q_{in} **b) With Q_{in}**

Fig. 6 Distributions of mole fractions along the symmetric line.

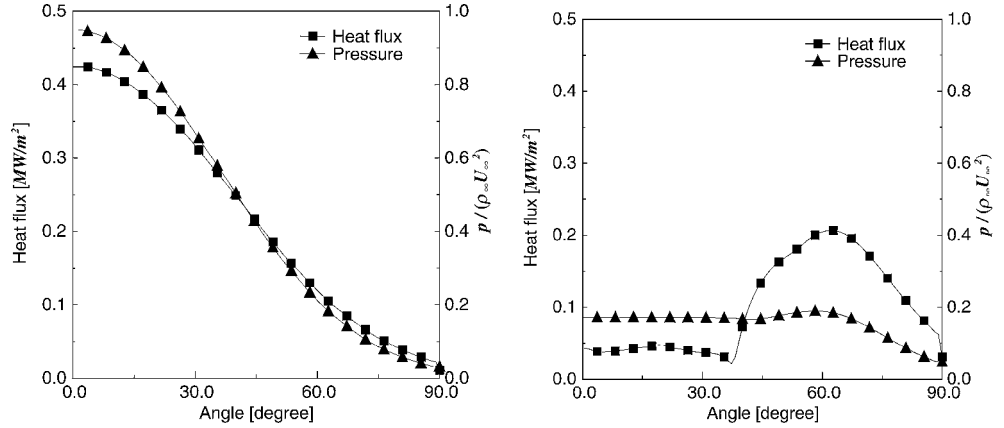

a) Without Q_{in} b) With Q_{in}

Fig. 7 Distributions of pressure and heat flux along the hemisphere surface.

drag becomes large in the outer region. Therefore, the case that has a peak at the outer region will show smaller drag than the case that has a peak close to the stagnation point even if the magnitudes of the peak pressure for both cases are the same. As a result of these factors, significant drag reduction can be realized.

Aerodynamic Characteristics

The results for the aerodynamic characteristics, drag, and the aerodynamic heating are presented here. C_D and $\dot{Q}$ indicate the drag coefficient and the heating rate, respectively, and are defined as follows:

$$C_D = \frac{\int_S F_x \, \mathrm{d}s}{\frac{1}{2}\rho_\infty V_\infty^2 S_0}, \qquad S_0 = \pi R^2 \tag{3}$$

$$\dot{Q} = \int_s \dot{q} \, \mathrm{d}s \tag{4}$$

where $\int_S$ means integration along the surface of the hemisphere. To measure the benefits of using heat release, we will use ratios of parameters to those without heat release. First, we define

$$C_D/C_{D0}, \qquad \dot{Q}/\dot{Q}_0 \tag{5}$$

where subscript 0 means the case without heat release. Also the efficiency of reduction for both parameters is considered:

$$\Delta C_D/C_{D0}E_c, \qquad \Delta\dot{Q}/\dot{Q}_0 E_c \tag{6}$$

where

$$\Delta C_D = C_{D0} - C_D, \qquad \Delta\dot{Q} = \dot{Q}_0 - \dot{Q} \tag{7}$$

Because the purpose of adding heat release to the flow is to gain aerodynamic improvement, the cases where $\Delta C_D < 0$ or $\Delta\dot{Q} < 0$ show degradation from the baseline and thus are not considered. We also use a simple combination rule

$$\tfrac{1}{2}(\Delta C_D/C_{D0} + \Delta\dot{Q}/\dot{Q}_0) \tag{8}$$

as an evaluation criterion for the total aerodynamic characteristics. Different (or more complex) formulations might be used, depending on design objectives for the high-speed vehicles. However, we will use this simple formulation in this work.

Unsteadiness

We obtained steady-state solutions in almost all cases. Some cases were in an unsteady or a periodic state. Here "unsteady" means that a solution has periodic perturbation, and it can be described as a quasi-steady state. In this calculation time accuracy was not considered because a local time-stepping method was used. Therefore instantaneous results did not have a time-accurate meaning. However, grid cell size does not change appreciably in the inviscid flow region, and time-averaged values of aerodynamic characteristics were thought to be worth evaluating. For this reason time-averaged values were used to discuss the results for such nonsteady state cases. In the following figures a symbol with an error bar will be used to describe this unsteady perturbation. An unsteady result whose perturbation is larger than 1% of its own value is plotted with an error bar. The error bar shows a maximum and minimum value of the periodic state.

In what follows we will discuss the effects of three parameters, x_c, E_c, and L, which are used to describe the heat source, on the aerodynamic drag and heating rate.

Parameter x_c

Figure 8 shows the correlation between the aerodynamic characteristics and the parameter x_c, the distance between the center of the heat source, and the stagnation point of the hemisphere. There are three sets of calculations generated by varying the parameter L: 0.1, 0.2, and 0.4. In all sets E_c is fixed at 0.01. The dotted line in Fig. 8 indicates the baseline result in which no heat release is present. As for the drag coefficient, all cases appearing in Fig. 8a show reduction of the drag. But the heating rate for some cases is not reduced. However, both the drag coefficient and the heating rate decrease as the parameter x_c increases, or the heat source moves further away from the body. This tendency of reduction stops, reaching an asymptotic value, when x_c roughly exceeds the value of 14.0. This indicates that no further aerodynamic benefits can be drawn by moving the heat source farther away from the body.

Parameter E_c

Figure 9 shows the effects of the heating rate on the aerodynamic characteristics. The horizontal axis shows the parameter E_c, the amount of energy supplied. Again, the dotted line in Fig. 9 shows the value corresponding to the flow without heat release. In these calculations the parameter L is varying but the parameter x_c is fixed to 4.0. We see that the drag coefficient in all cases appearing in Fig. 9a has been reduced. The drag decreases as the heat release increases, and the tendency of the reduction ratio seems to be independent of the parameter L. Some calculations with larger values of heat release like $E_c = 10$ are conducted; these results show that excessive heat release may in fact have an adverse effect on the heating rate $\dot{Q}/\dot{Q}_0$ and might even increase the drag (not included in Fig. 9a). Nevertheless, this large amount of heat release results in a maximum temperature well above 30,000 K, making the validity of the physical models questionable. These cases are denoted by the symbol $\times$ in Table 3.

Regarding the heating rate, reduction from the baseline value has been achieved in some cases. It is obvious that when heat release is directly added to the free stream enthalpy the hemisphere can experience high heating unless the flow structure is altered. Figure 9 demonstrates that an excessive amount of heat release increases the heating rate. On the other hand, if an appropriate amount of heat release occurs in front of the body then the heating rate can be reduced.

Figure 9 also shows the correlation between the efficiency of both the aerodynamic parameters and the parameter E_c. An obvious reduction is found for the efficiency of drag coefficient, and

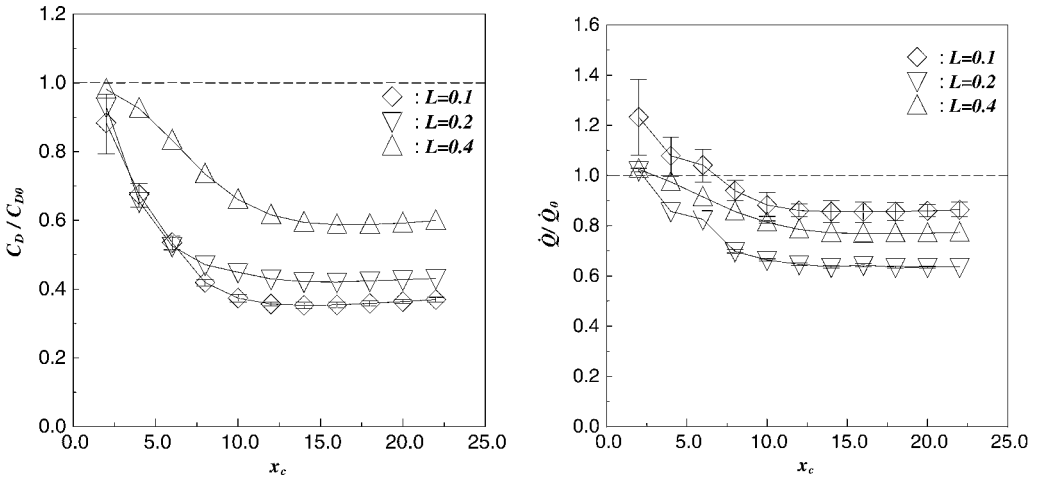

a) Drag coefficient b) Heating rate

Fig. 8 Correlation to the parameter x_c.

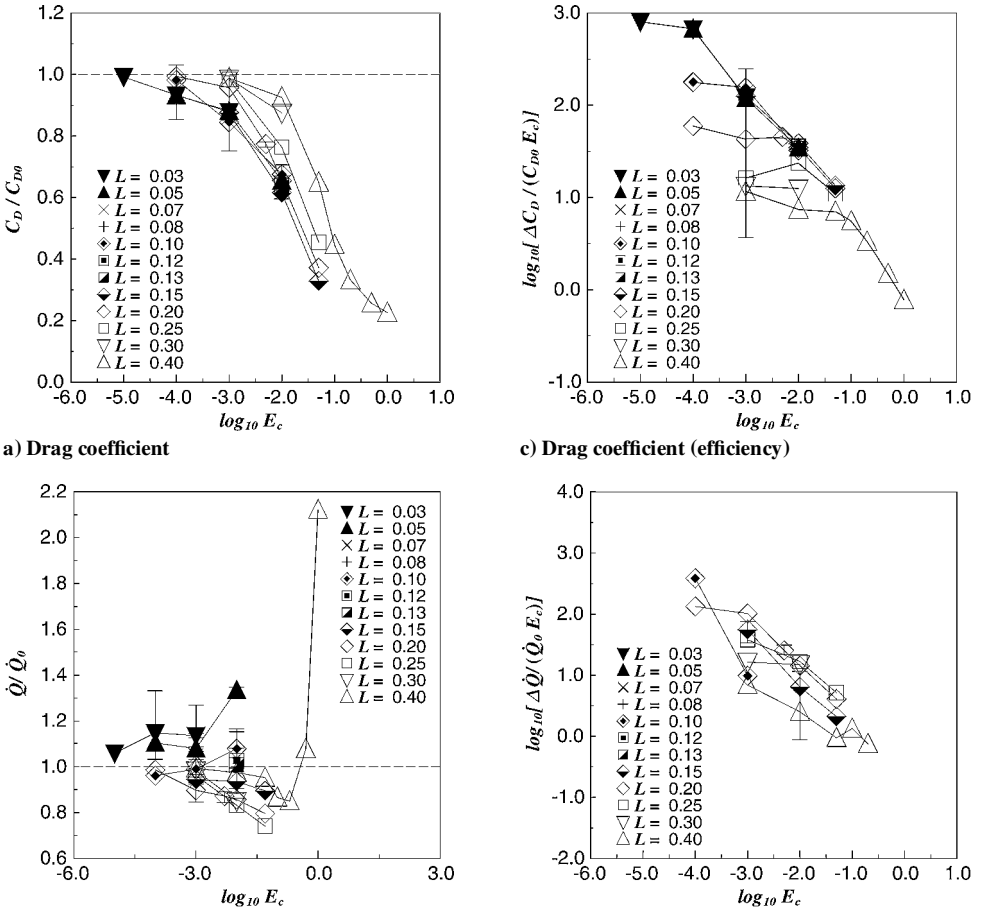

a) Drag coefficient c) Drag coefficient (efficiency)

b) Heating rate d) Heating rate (efficiency)

Fig. 9 Correlation to the parameter E_c.

interestingly it appears to have two distinct rates of dependence on E_c.

The efficiency for a relatively small heat release decreases gradually as the parameter E_c increases. But with a greater heat release the efficiency not only decreases rapidly, but also appears to be independent of the parameter L because all cases collapse onto a single line. When analyzing the heating rate in Fig. 9d, we also see a general trend in that the efficiency decreases as the parameter E_c increases, nearly at the same rate for different values of L.

Parameter L

Figure 10 shows the influences of the parameter L, a measure of the size (length scale) of the heat source. In Fig. 10a all cases show a reduction in the drag. For $L \geq 0.15$ the drag increases as L increased. On the other hand, when L is under 0.15 (suggesting a more focused heat source) the effect of L seems rather mild. As the heat source becomes smaller, it makes the primary shock wave stronger, resulting in a greater change (higher pressure than that without heat release) in the flow behind the heat release region. For example, Fig. 11 shows the dynamic pressure distribution along the plane of $x = 2.5$. Near the center (where the distance is small) the dynamic pressure is smaller than its freestream value and moreover decreases with L, i.e., the more deficit of dynamic pressure it becomes. As this high-pressure stream flows onto the body, the pressure at the forward portion of the body gets higher and thus reverses the trend of reduction as L decreases. Nevertheless,

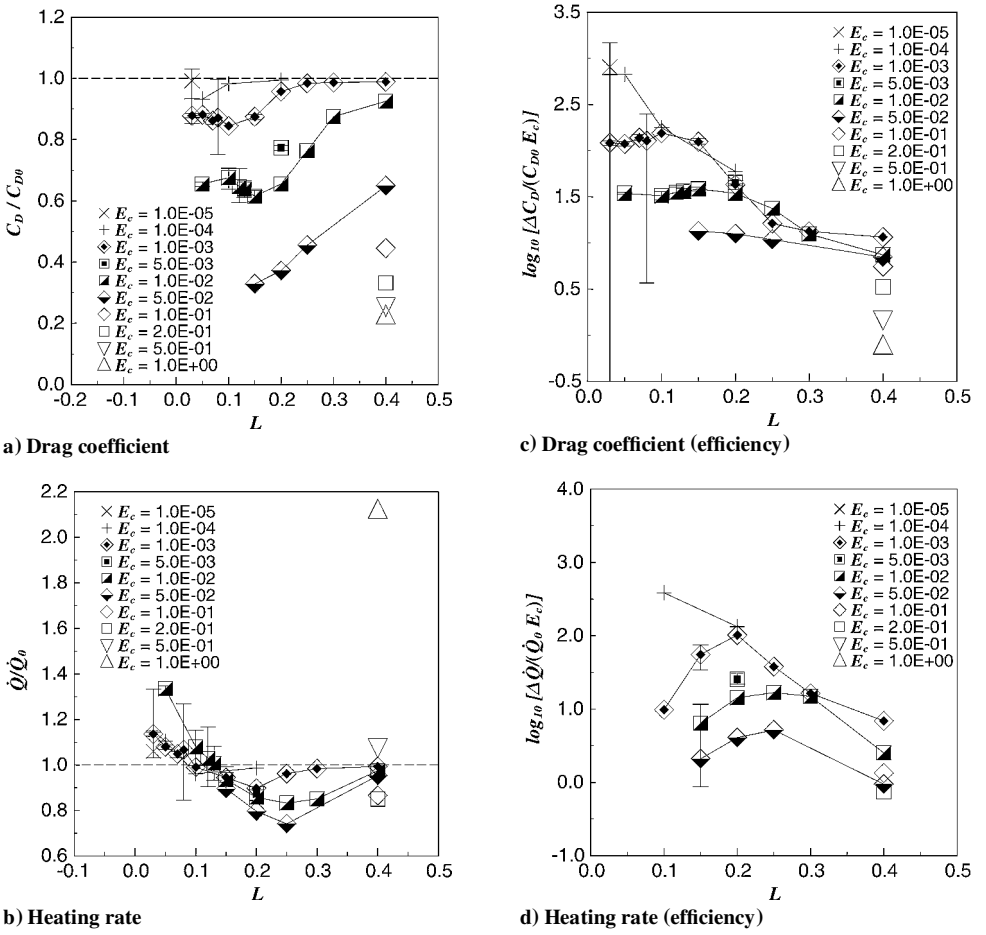

Fig. 10 Correlation to the parameter L.

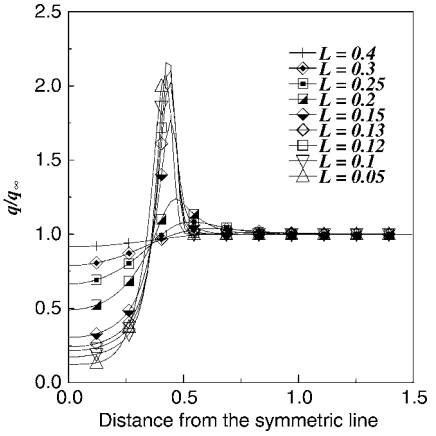

Fig. 11 Distributions of the dynamic pressure along the r direction at $x = 2.5$ as changing L.

an optimum value of L seems to exist for each E_c, at least for $E_c < 5.0 \times 10^{-2}$.

As for the heating rate, there is a range of values of L for which a reduction in heating rate can be realized and an optimum value of L for a given E_c clearly exists. The cases with smaller values of the parameter L show an increase of the heating rate, even beyond the baseline value (without the heat release). The larger value of L indicates that heat release is dispersed and has less influence on the freestream state.

Figure 10 also shows the correlation between the efficiency of both parameters and the parameter L. As for the drag coefficient, the trend in efficiency is similar to that of the parameter E_c; we again see two distinct rates of dependence on L. For smaller L the efficiency is essentially independent of L; but for larger L the efficiency decreases nearly linearly as L increases. Moreover, the results for a group of small values of E_c appear to collapse onto a single line as $L \geq 0.25$. If the parameter L becomes large, the primary shock and temperature layer become weak, and they does not affect the aerodynamic characteristics of the hemisphere. In other words, a great amount of heat release is necessary in such large value of L, and it means that the primary shock and temperature layer are located far from the symmetric axis. Therefore the outer part of the heat source does not affect the aerodynamic characteristics of the hemisphere, and the efficiency of heat release can be expected to decline. Concerning the heating rate, L yields an optimum efficiency, which varies according to the values of E_c. These optimum values of L are similar to the optimum values of the heating rate.

Table 4 Remarkable values

x_c (fixed)	L	E_c	C_D/C_{D0}	$\dot{Q}/\dot{Q}_0$	$\frac{1}{2}(\dot{Q}/\dot{Q}_0 + C_D/C_{D0})$
4.0	0.4	1.0	0.22598 (23%)	2.12083	1.173405
4.0	0.25	0.05	0.45512	0.74094 (74%)	0.598035
4.0	0.2	0.05	0.37196	0.79623	0.584095 (58%)

Remarkable Values

Some results obtained with a fixed value of the parameter $x_c = 4.0$ are listed in Table 4. For example, the condition with the parameters $L = 0.4$ and $E_c = 1.0$ gives a remarkable drag reduction, attaining a value of 23% of C_{D0}. Similarly, we find that the heating rate is reduced to 74% by choosing $L = 0.25$ and $E_c = 0.05$, and the combined parameter reduced to 58% if $L = 0.2$ and $E_c = 0.05$.

Reduction Mechanism

The flowfields altered by heat release can become very complex because of the shock-shock or shock-temperature layer interactions, and it is not straightforward to delineate the influences of the parameters involved. However, we will attempt to suggest a mechanism

that appears to be uniformly dominant for the range of parameters studied. We will mainly focus on the drag reduction mechanism and its correlation to the parameter x_c in this paper. The reduction mechanism of the heating rate or the role of other parameters will be discussed in separate papers.

The modified Newtonian theory can accurately predict pressure distributions on the hemisphere when the flow is supersonic or hypersonic and is described as follows:

$$p_\theta = (p_t - p_\infty)\cos^2\theta + p_\infty \tag{9}$$

Moreover, the stagnation pressure on the hemisphere is nearly equal to the total pressure behind the normal shock p_t:

$$p_{\text{stagnation}} \sim p_t \tag{10}$$

And p_t comes from an alternative expression for the Rayleigh pitot formulation with perfect gas assumption,

$$p_t = p_\infty\left(\frac{\gamma+1}{2}M_\infty^2\right)^{\gamma/(\gamma-1)}\left[\frac{\gamma+1}{2\gamma M_\infty^2-(\gamma-1)}\right]^{1/(\gamma-1)} \tag{11}$$

$$\sim 1.29 p_\infty M_\infty^2 \quad (\gamma = 1.4,\ M_\infty \gg 1)$$

$$\sim q_\infty \ (= \text{dynamic pressure}) \tag{12}$$

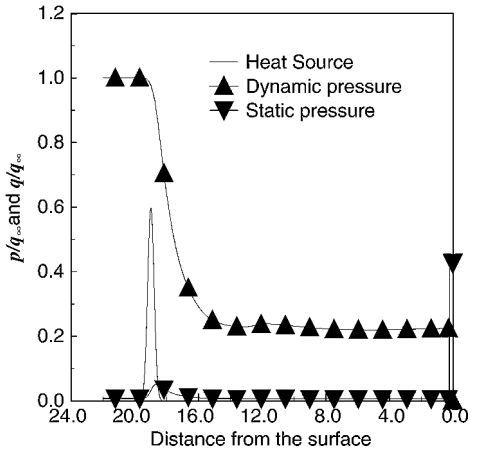

Fig. 12 Distributions of the static and dynamic pressure along the symmetric line ($x_c = 20$, $L = 0.2$, and $E_c = 0.01$).

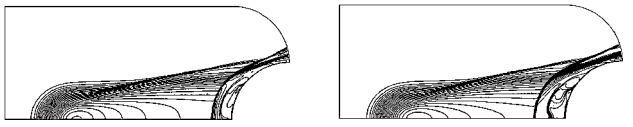

a) With high-temperature effects **b) With perfect gas assumption**

Fig. 13 Temperature contours for parameters $x_c = 4.0$, $L = 0.2$, and $E_c = 0.05$.

which says that the surface pressure is a function of the dynamic pressure q_∞ in front of the bow shock. Figure 12 shows the distribution of dynamic pressure along the symmetric axis for a typical flow with heat release, showing a dynamic pressure decrease behind the heat release region. This occurs because the flow behind the heat release region undergoes an expansionlike process, resulting in a drop in dynamic pressure, which is further reduced by the bow shock. Consequently, the surface pressure on the body is reduced, thus resulting in drag reduction. The longer the distance between the heat source and the hemisphere or the larger the parameter x_c is, the more the dynamic pressure before the bow shock decreases, resulting in greater drag reduction. The dynamic pressure decreases rapidly around the heat release region and then saturates, coinciding with saturation of the drag reduction for large values of x_c.

High-Temperature Effects

Two cases are considered to demonstrate high-temperature effects in this study. In each case results calculated without high-temperature effects (with perfect gas assumption) are compared with those including the high-temperature effects. Consider the case that has been mentioned before whose parameters are $x_c = 4.0$, $L = 0.2$, and $E_c = 0.05$. The temperature contours of Fig. 13 clearly illustrate different shock configurations for the two flow cases. In the absence of high-temperature effects, the bow shock is located further upstream, and the primary shock resides slightly farther away from the symmetric line. Corresponding surface pressure and heat-flux distributions shown in Fig. 14 indicate a significant reduction in the heat flux peak as a result of high-temperature effects, with a consequent reduction in surface heating by a factor of 2.5. On the contrary, drag is slightly increased by the high-temperature effects by approximately 15%.

For the next parameter set with smaller L and E_c, $x_c = 4.0$, $L = 0.05$, $E_c = 0.001$, differences between the two flow cases are more pronounced than that of preceding set of parameters. Bow shock behavior is qualitatively similar to that observed earlier, as shown in the temperature contours of Fig. 15; however, surface pressure and heat-flux distributions show very different trends in shape, peak locations, and values, as shown in Fig. 16. These differences mainly come from the difference in primary shock configuration. This result clearly demonstrates that high-temperature effects can cause considerable changes in shock configuration, surface heat flux and surface pressure, and thus should not be ignored in the prediction of drag and heating rate.

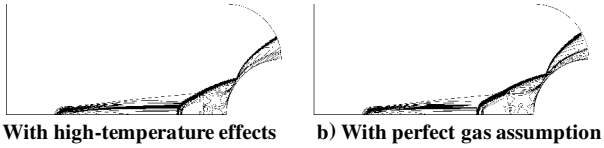

a) With high-temperature effects **b) With perfect gas assumption**

Fig. 15 Temperature contours for parameters $x_c = 4.0$, $L = 0.05$, and $E_c = 0.001$.

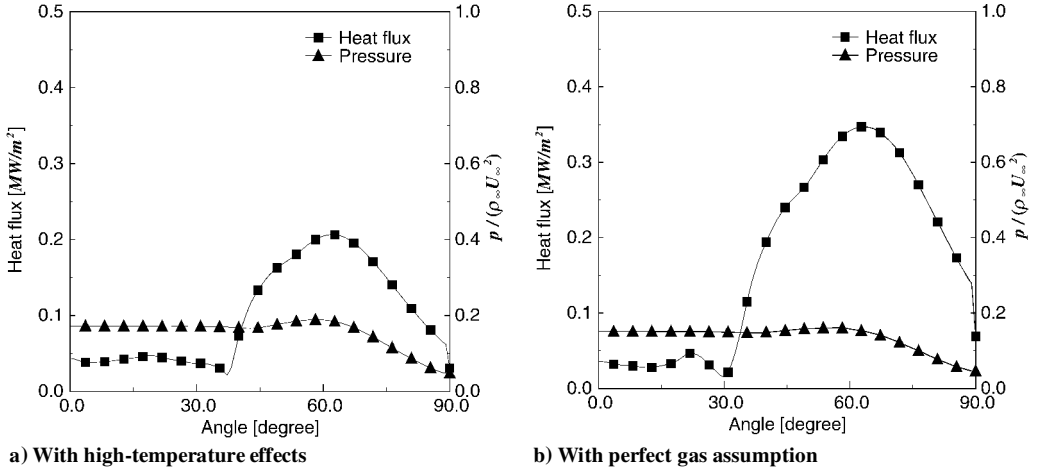

a) With high-temperature effects **b) With perfect gas assumption**

Fig. 14 Distributions of pressure and heat flux along the hemisphere surface for parameters $x_c = 4.0$, $L = 0.02$, and $E_c = 0.05$.

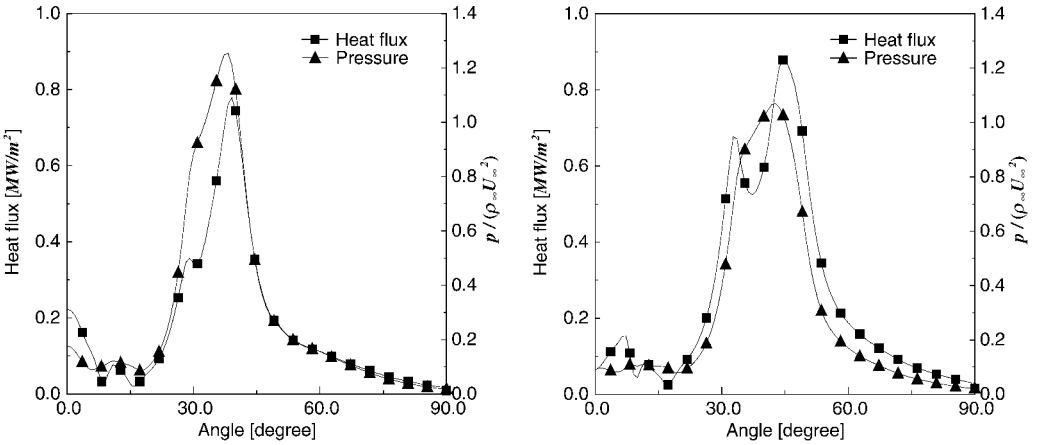

a) With high-temperature effects **b) With perfect gas assumption**

Fig. 16 Distributions of pressure and heat flux along the hemisphere surface for parameters $x_c = 4.0$, $L = 0.05$, and $E_c = 0.001$.

Conclusions

This paper provides a parametric study of hypersonic flows around a hemisphere with heat release. The flows were numerically analyzed with the high-temperature effects, including chemical and thermal nonequilibrium effects. This investigation has shown that heat release in front of the hemisphere can reduce both drag and surface heating rate. Three parameters—the location of the heat source, the characteristic length of the heat source, and the amount of the heat supplied—are introduced to characterize and evaluate the feasibility of this new concept. Two important aerodynamic parameters for hypersonic flight, drag coefficient and heating rate, are used as criteria to systematically evaluate the effects of these three parameters.

An increase of the distance of the heat source from the hemisphere makes the aerodynamic drag and the aerodynamic heating rate decrease monotonically. This reduction, however, saturates if the distance between the heat source and the hemisphere becomes longer than 14 times the length of the radius of the hemisphere. Increasing of the amount of the heat release makes the aerodynamic drag decrease monotonically in the range of the parameters studied. As for the aerodynamic heating rate, an appropriate amount of input energy can reduce the heating rate. Increasing of the characteristic length of the heat source makes the aerodynamic drag increase in general and the aerodynamic heating rate decrease at first then increase. Hence, an optimum length exists for both parameters.

The aerodynamic drag can be reduced down to 23% of its value without heat release, whereas the aerodynamic heating rate can be reduced to 74% of the base value. These values can be reduced to 37 and 80%, respectively, at the same time. These results have been obtained without any optimization methods, and better results might be possible with the optimization methods.

The dynamic pressure plays an important role in the drag-reduction mechanism. The surface pressure is a function of the dynamic pressure in the freestream, and the heat release in the upstream region makes the dynamic pressure decrease. Consequently, the heat release can result in a reduction of the aerodynamic drag on the body.

There seems to exist optimum conditions for simultaneously achieving minimum aerodynamic drag and heating rate. Hence, coupling the CFD calculation with an optimization method might be useful for a future investigation.

References

[1]Bogdonoff, S., and Vas, I., "Preliminary Investigations of Spiked Bodies at Hypersonic Speeds," *Journal of Aerospace Sciences*, Vol. 26, No. 2, 1959, pp. 65–74.

[2]Crawford, D., "Investigations of the Flow over a Spiked-Nose Hemisphere-Cylinder," NASA TN D-118, Dec. 1959.

[3]Maull, D., "Hypersonic Flow over Axially Symmetric Spiked Bodies," *Journal of Fluid Mechanics*, Vol. 8, No. 4, 1960, pp. 584–592.

[4]Wood, C., "Hypersonic Flow over Spiked Cones," *Journal of Fluid Mechanics*, Vol. 12, No. 4, 1961, pp. 614–624.

[5]Myrabo, L., and Raizer, Y., "Laser-Induced Air Spike for Advanced Transatmospheric Vehicles," AIAA Paper 94-2451, June 1994.

[6]Marconi, F., "An Investigation of Tailored Upstream Heating for Sonic Boom and Drag Reduction," AIAA Paper 98-0333, Jan. 1998.

[7]Levin, V., and Terentéva, L., "Supersonic Flow over a Cone with Heat Release in the Neighborhood of the Apex," *Izvestiya Rossiiskoi Akademii Nauk, Mekhanika Zhidkosti i Gaza*, Vol. 31, No. 2, 1993, pp. 110–114.

[8]Riggins, D., Nelson, H., and Johnson, E., "Blunt-Body Wave Drag Reduction Using Focused Energy Deposition," *AIAA Journal*, Vol. 37, No. 4, 1999, pp. 460–467; also AIAA Paper 98-1647, April 1998.

[9]Golovitchev, V., and Hansson, J., "Some Trends in Improving Hypersonic Vehicles Aerodynamics and Propulsion," *Proceedings of 14th International Symposium on Air-Breathing Engines*, ISABE Paper 99-7088, Florence, Italy, Sept. 1998.

[10]Takaki, R., and Wada, Y., "Numerical Simulation of High Enthalpy Flow—High Enthalpy Flow Workshop," *Proceedings of 13th National Aerospace Laboratory Symposium on Aircraft Computational Aerodynamics—High Enthalpy Flow Workshop*, National Aerospace Lab., NAL SP-29, Tokyo, 1996, pp. 171–177.

[11]Gnoffo, P., Gupta, R., and Shinn, J., "Conservation Equations and Physical Models for Hypersonic Air Flows in Thermal and Chemical Nonequilibrium," NASA TP-2867, Feb. 1989.

[12]Park, C., "Assessment of a Two-Temperature Kinetic Model for Dissociating and Weakly-Ionizing Nitrogen," *Journal of Thermophysics and Heat Transfer*, Vol. 2, No. 1, 1988, pp. 8–16; also AIAA Paper 86-1347, June 1986.

[13]Park, C., and Yoon, S., "A Fully-Coupled Implicit Method for Thermo-Chemical Nonequilibrium Air at Sub-Orbital Flight Speeds," *Journal of Spacecraft and Rockets*, Vol. 28, No. 1, 1991, pp. 31–39; also AIAA Paper 89-1974, June 1989.

[14]Millikan, R., and White, D., "Systematics of Vibrational Relaxation," *Journal of Chemical Physics*, Vol. 39, No. 12, 1963, pp. 3209–3213.

[15]Park, C., "Problems of Rate Chemistry in the Flight Regimes of Aeroassisted Orbital Transfer Vehicles," AIAA Paper 84-1730, June 1984.

[16]Wada, Y., and Liou, M., "A Flux Splitting Scheme with High-Resolution and Robustness for Discontinuities," AIAA Paper 94-0083, Jan. 1994.

[17]Wada, Y., and Liou, M., "An Accurate and Robust Flux Splitting Scheme for Shock and Contact Discontinuities," *SIAM Journal on Scientific and Statistical Computing*, Vol. 18, No. 3, 1997, pp. 633–657.

M. Sichel
Associate Editor